

Fabrication of Metal-Doped Hierarchical Trimodal Porous $\text{Li}_3\text{V}_2(\text{PO}_4)_3/\text{C}$ Composites with Enhanced Electrochemical Performances for Lithium-Ion Batteries



HE WANG, LONGFANG LI, SHULAN WANG, XUAN LIU, and LI LI

Na/Cr-doped $\text{Li}_3\text{V}_2(\text{PO}_4)_3/\text{C}$ composites with a hierarchical trimodal porous structure, including micro-, meso-, and macropores, are synthesized by a feasible ice-templating method and investigated as cathodes for lithium-ion batteries (LIBs). Na and Cr doping decrease the charge transfer resistance of $\text{Li}_3\text{V}_2(\text{PO}_4)_3/\text{C}$ and increase the diffusion coefficient of Li ions within the three-dimensional interconnected network, resulting in enhancement of both the capacity and rate performances of hierarchical porous $\text{Li}_3\text{V}_2(\text{PO}_4)_3/\text{C}$ with maximized electrochemical performances at a doping level of $x = 0.04$. Cr doping shows a higher enhancement than Na in the capacity of $\text{Li}_3\text{V}_2(\text{PO}_4)_3$. As-prepared Cr-doped $\text{Li}_3\text{V}_{1.96}\text{Cr}_{0.04}(\text{PO}_4)_3/\text{C}$ shows the high capacity and rate performance of 116.8 mAh g^{-1} at 10 C as well as an excellent cyclability. This work provides a simple and feasible method to fabricate metal-doped hierarchical trimodal porous cathode materials and deepens our understanding on design of high-performance electrode materials for LIBs.

<https://doi.org/10.1007/s11661-018-5075-4>

© The Minerals, Metals & Materials Society and ASM International 2019

I. INTRODUCTION

LITHIUM-ION batteries (LIBs) have attracted broad attention due to their high energy and power densities, long lifespans, wide operating temperature, and environmental benignity.^[1–3] Layered- LiCoO_2 and spinel- LiMn_2O_4 are the first commercial cathode materials for LIBs but have some limitations for large-scale applications due to their high cost, low safety, and toxicity.^[4–6] Transition-metal phosphate $\text{Li}_3\text{V}_2(\text{PO}_4)_3$ (LVP) has attracted considerable interest as the cathode materials for rechargeable LIBs due to its intrinsic structural and chemical stability brought by the three-dimensional polyanion $(\text{PO}_4)^{3-}$ framework, a wide insertion/extraction voltage of 4.0 V (~ 0.6 V higher than LiFePO_4), and a high theoretical capacity (133 mAh g^{-1} in the potential range of 3.0 to 4.3 V).^[7] Nevertheless, LVP still faces challenges such as a negligible electronic conductivity ($2.4 \times 10^{-7} \text{ S cm}^{-1}$)

and a low ionic conductivity due to the intrinsic separated VO_6 octahedral arrangement.^[8,9] To address this issue, many methods have been explored, including doping with metal ions,^[5,10,11] surface coating with conductive materials,^[12] introducing other oxides,^[13] and reducing particle sizes of the active materials.^[14] Metal ion doping is viewed as an effective approach to improve the microstructure and charge transfer as well as electrochemical performances of LVP.^[15] To date, many metal ion dopants, including K^+ , Fe^{3+} , Ni^{2+} , Al^{3+} , Zn^{2+} , Mg^{2+} , Ca^{2+} , and B^{3+} , have been investigated for replacing V^{3+} or Li^+ in LVP.^[8,10,16–20] K-doped LVP with N-doping carbon coating $\text{Li}_{2.99}\text{K}_{0.01}\text{V}_2(\text{PO}_4)_3/\text{C} + \text{N}$ shows an enhanced conductivity and electrochemical performance.^[8] Al-substituted C- $\text{Li}_3\text{V}_{1.98}\text{Al}_{0.02}(\text{PO}_4)_3$ cathode displays a high discharge capacity of 182 mAh g^{-1} in the potential range of 3 to 4.8 V.^[10] The discharge capacity of B-doped $\text{Li}_3\text{V}_2(\text{P}_{0.97}\text{B}_{0.03}\text{O}_4)_3/\text{C}$ is as high as 130 mAh g^{-1} , with a high capacity retention of 98 pct after 100 cycles.^[20] Surface carbon coating can reduce contact resistances between the LVP active material and the electrolyte to achieve enhanced electrochemical performances and, therefore, is considered as a feasible and economic method.^[21–23] However, most conventional carbon loading methods are limited to nanoscales, while hierarchical pore structures, including micro-, meso-, and macropores, are highly desirable structures that can provide fast transport channels of charges and

HE WANG, LONGFANG LI, SHULAN WANG, and XUAN LIU are with the Department of Chemistry, School of Science, Northeastern University, Shenyang 110819, P.R. China. Contact emails: slwang@mail.neu.edu.cn, xuanliucmu@gmail.com LI LI is with the School of Metallurgy, Northeastern University, Shenyang 110819, P.R. China. Contact emails: lilicmu@alumni.cmu.edu, lilicmu@gmail.com

Manuscript submitted August 15, 2018.

Article published online January 1, 2019

result in enhancement of the electrochemical performances of the materials.^[24]

Herein, Na- and Cr-doped hierarchical porous LVP/C composite materials with full trimodal pores were synthesized by the ice-templating method with influence from the doping content on the morphology, structure, and electrochemical performance as well as the charge storage mechanism of LVP/C investigated. Complex synthesis steps in most conventional templating methods were avoided in the present work.

II. EXPERIMENTAL

Citric acid, $(\text{NH}_4)_2\text{HPO}_4$, and V_2O_5 were added in sequence into deionized water at 80°C under continuously stirring until an orange color was achieved. Both Li_2CO_3 and Na_2CO_3 (or Cr_2O_3) were introduced to the preceding solution under stirring to form a dark blue solution. The solution was then immersed into liquid nitrogen for complete freeze followed with freeze drying in vacuum. The dark blue powders collected after freeze drying were preheated at 300°C for 4 hours to remove CO_2 , NH_3 , and H_2O and then further heated at 800°C to 900°C for 12 hours in Ar atmosphere for sample formation. All reagents are of analytical grade and are commercially available (Sinopharm Company, China). The molar ratio between $(\text{NH}_4)_2\text{HPO}_4$, V_2O_5 , and Li_2CO_3 in all samples is controlled to be 3:2:3. Scheme 1 illustrates the fabrication process flow of the hierarchical porous LVP/C composites.

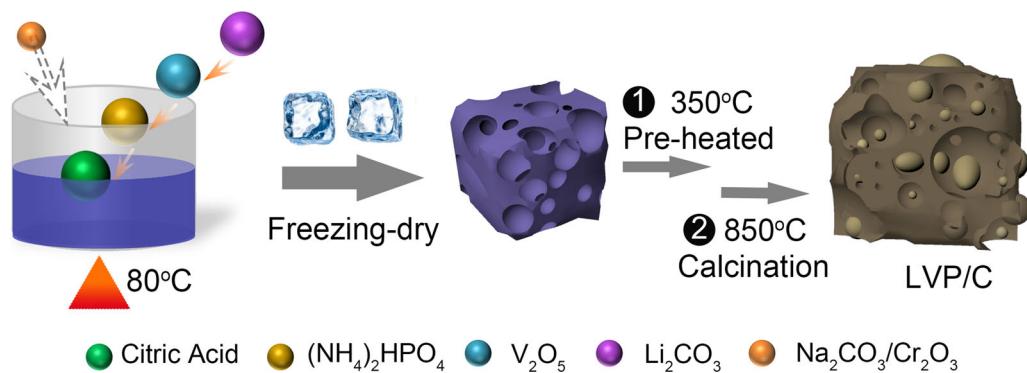
The crystal structure of the samples was measured with X-ray diffraction (XRD) using an X'Pert Pro diffractometer (PANalytical B.V., Netherlands). Surface morphology and elemental distribution were obtained by scanning electron microscopy (SEM) and energy-dispersive spectroscopy (Ultra Plus, Carl Zeiss, Germany). Transmission electron microscopy (TEM, JEM-2100) images with a high resolution were taken to illustrate the porous structure. Thermogravimetric and differential thermal analysis (TG/DTA) were conducted in N_2 atmosphere at a heating rate of $10^\circ\text{C}/\text{min}$ from 27°C to 900°C using a thermal analyzer (METTLER TOLEDO-3). Raman spectroscopy was carried out by

LabRAM HR 800 to examine the chemical composition. The electron binding energy of elements in the samples was analyzed by XPS (PHI 5600) using monochromatic Al K_{α} X-rays (350 W) with a pass energy of 29 eV. The surface area and pore volume were tested by Brunauer-Emmett-Teller (BET) analysis at $P/P_0 = 0.99$ point.

Electrochemical performances of the samples were studied as a Li-ion half-cell with the samples assembled as CR2025 type coin cells in an argon-filled glove box. The samples were mixed with acetylene black and polyvinylidene fluoride in a weight ratio of 8:1:1, while some drops of the N-methyl pyrrolidone solution were added to form the slurry under stirring. The slurry was then uniformly pasted on an Al foil followed with vacuum drying at 130°C . The sample loaded on each Al foil was around 2.2 to $2.5\text{ mg}\cdot\text{cm}^{-2}$. A pure lithium foil was used as the anode and a porous polypropylene film (Celgard 2400) was used to separate the cathode and anode. The electrolyte was selected to be 1 M LiPF_6 in ethylene carbonate, dimethyl carbonate, and ethylene methyl carbonate (1:1:1 in the volumetric ratio). Galvanostatic charge/discharge curves were performed in the potential window of 3.0 to 4.3 V on a LAND CT2001A system (Wuhan, China). Cyclic voltammetry (CV) curves were recorded by the electrochemical workstation (EG&G Princeton Applied Research 273A) with scan rates of 0.05 to $0.3\text{ mV}\cdot\text{s}^{-1}$. Electrochemical impedance spectroscopy (EIS) was measured in a frequency range of 100 kHz to 0.01 Hz using Princeton 273A and 5210 Lock-in Amplifier with a perturbation amplitude of 5 mV.

III. RESULTS AND DISCUSSION

Powdered XRD patterns of intrinsic $\text{Li}_3\text{V}_2(\text{PO}_4)_3/\text{C}$ as well as doped samples ($\text{Li}_{3-x}\text{Na}_x\text{V}_2(\text{PO}_4)_3/\text{C}$ and $\text{Li}_3\text{V}_{2-x}\text{Cr}_x(\text{PO}_4)_3/\text{C}$ ($x = 0.03, 0.04, \text{ and } 0.05$)) annealed at 850°C are presented in Figure 1. All reflections can be indexed into well-defined LVP (PDF 80-1515) without any traces of impurities, indicating LVP was synthesized successfully while the addition of



Scheme 1—Illustration of fabrication flow of hierarchical porous Na/Cr-doped LVP/C nanocomposites.

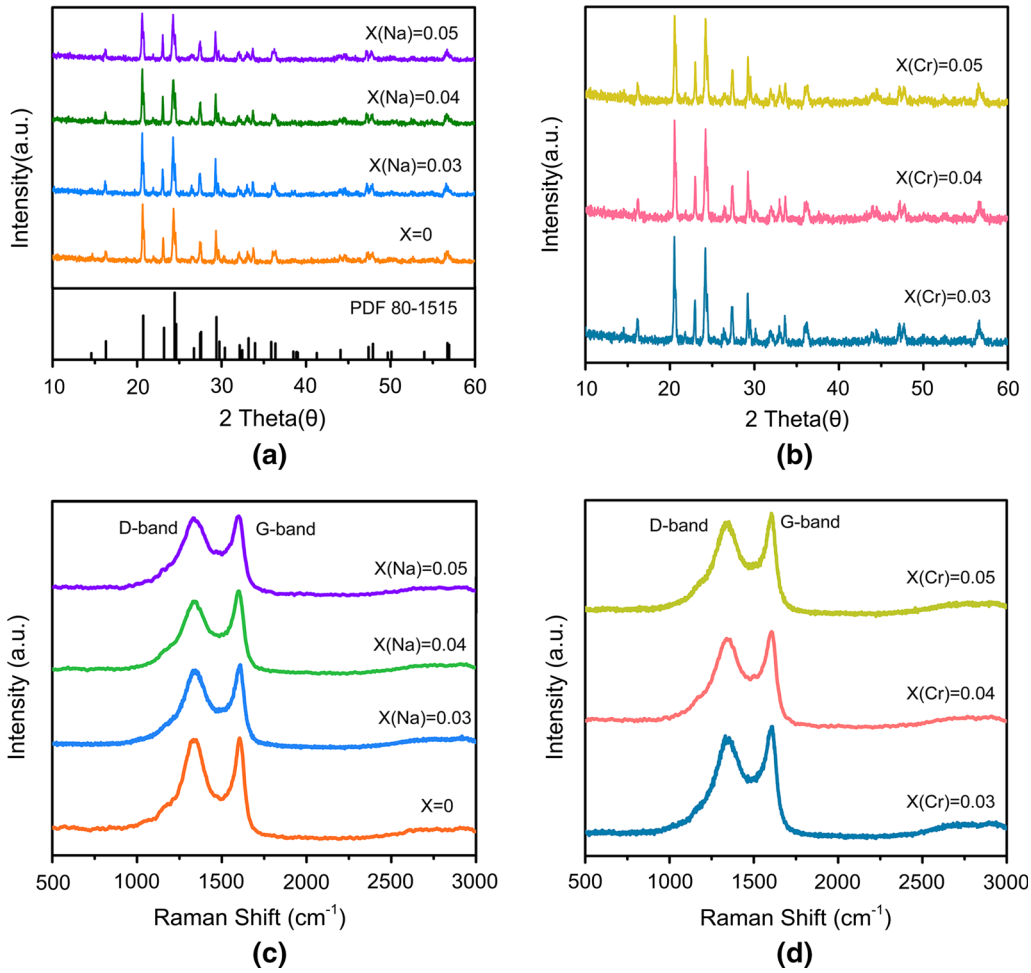


Fig. 1—XRD patterns of (a) $\text{Li}_{3-x}\text{Na}_x\text{V}_2(\text{PO}_4)_3/\text{C}$ and (b) $\text{Li}_3\text{V}_{2-x}\text{Cr}_x(\text{PO}_4)_3/\text{C}$ annealed at 850 °C. Raman spectra of (c) $\text{Li}_{3-x}\text{Na}_x\text{V}_2(\text{PO}_4)_3/\text{C}$ and (d) $\text{Li}_3\text{V}_{2-x}\text{Cr}_x(\text{PO}_4)_3/\text{C}$ ($x = 0, 0.03, 0.04, \text{ and } 0.05$).

Table I. Lattice Parameters of Na- and Cr-Doped $\text{Li}_3\text{V}_2(\text{PO}_4)_3/\text{C}$ Annealed at 850 °C

Sample	<i>A</i> (nm)	<i>B</i> (nm)	<i>C</i> (nm)	<i>V</i> _{cell} (nm ³)
$x_{\text{Na}} = 0.03$	0.85663	1.20086	0.86172	0.8864
$x_{\text{Na}} = 0.04$	0.85681	1.20102	0.86180	0.8868
$x_{\text{Na}} = 0.05$	0.85708	1.20139	0.86192	0.8875
$x_{\text{Cr}} = 0.03$	0.85586	1.20057	0.86048	0.8842
$x_{\text{Cr}} = 0.04$	0.85568	1.20037	0.86011	0.8834
$x_{\text{Cr}} = 0.05$	0.85547	1.20004	0.85989	0.8827
LVP/C	0.85630	1.20083	0.86149	0.8858
80-1515	0.8562	1.2005	0.8612	0.8852

Na and Cr dopants did not change the monoclinic structure of LVP. The sharp peaks of XRD patterns with high intensities reflect the high crystallinity degree of LVP. The change in the lattice parameters with the dopant content was investigated for $\text{Li}_{3-x}\text{Na}_x\text{V}_2(\text{PO}_4)_3$ and $\text{Li}_3\text{V}_{2-x}\text{Cr}_x(\text{PO}_4)_3$ ($x = 0, 0.03, 0.04, \text{ and } 0.05$) samples, and the results are presented in Table I. Jade 6.0 software was used for calculation of the lattice parameters. Both Na and Cr doping lead to lattice

distortion of LVP. The cell parameters and cell volumes of Na-doped LVP/C composites are larger than those of pristine LVP/C and increase slightly with the increase in the doping level of Na. Na^+ ($r = 0.102$ nm) has a larger radius than Li^+ ($r = 0.068$ nm), so substitution of Li^+ with Na^+ expands the cell volume of LVP, resulting in a broader space in the crystal structure of LVP to facilitate Li-ion diffusion and transportation.^[25] In contrast, substitution of V^{3+} (0.074 nm) with Cr^{3+} (0.064 nm) in $\text{Li}_3\text{V}_{2-x}\text{Cr}_x(\text{PO}_4)_3$ leads to the shrinkage of lattice constants and contraction of cell volumes of LVP.^[4]

Figures 1(c) and (d) exhibit the Raman shift of all samples with two primary peaks at 1345 cm^{-1} (D band) and 1607 cm^{-1} (D band) that are related to disordered and graphitic carbon, respectively. All samples show close I_G/I_D values, which indicates that they have similar graphitic degree. The electrical conductivity of $\text{Li}_{3-x}\text{Na}_x\text{V}_2(\text{PO}_4)_3/\text{C}$ and $\text{Li}_3\text{V}_{2-x}\text{Cr}_x(\text{PO}_4)_3/\text{C}$ obtained by the four-probe method is much higher than LVP/C (0.043 S cm^{-1}) and is 0.125, 0.166, and 0.125 S cm^{-1} for $x_{\text{Na}} = 0.03, 0.04, \text{ and } 0.05$ and 0.077, 0.25, and 0.125 S cm^{-1} for $x_{\text{Cr}} = 0.03, 0.04, \text{ and } 0.05$, respectively.

In the doped and undoped samples annealed at 850 °C, there are large macropores with diameters about 0.1 to 0.5 μm and small mesopores in the interconnected walls (Figure 2). The macropores are primarily introduced through freeze casting by ice templation, while the mesopores may arise from decomposition of Li_2CO_3 and $(\text{NH}_4)_2\text{HPO}_4$ and the release of gaseous products during pyrolysis.^[26] The addition of dopants apparently did not influence the morphology of the as-prepared materials. The combination of abundant macropores/mesopores can accommodate the stress induced by lithium insertion and extraction.^[27,28]

The morphology and microstructure of $\text{Li}_{2.96}\text{Na}_{0.04}\text{V}_2(\text{PO}_4)_3/\text{C}$ and $\text{Li}_3\text{V}_{1.96}\text{Cr}_{0.04}(\text{PO}_4)_3/\text{C}$ were further investigated by bright-field and high-resolution TEM (Figure 3). A hierarchical trimodal porous structure, including micro-, meso-, and macropores, was observed in both samples. The SAED patterns in the insets of Figures 3(b) and (e) indicate the high crystallinity of the as-prepared electrode materials.^[29] HRTEM images, as presented in Figures 3(c) and (f), show a uniform thin carbon layer with a thickness of 5 nm coated on the surface of LVP, in which carbon can timely dissipate electrons and enhance transportation of charges and ions within the interconnected structure. The lattice fringe of the crystalline material is measured to be 0.38 nm, corresponding to the (210) plane of monoclinic $\text{Li}_3\text{V}_2(\text{PO}_4)_3$.

The thermal behavior of as-prepared LVP/C samples is analyzed with TG/DTA under N_2 flow at a heating rate of 10 °C min^{-1} , and the result is shown in Figure 4(a). The rapid weight loss between 67 °C and 112 °C is related to the release of physically adsorbed water and accompanied by the endothermic at 125 °C. The significant weight loss between 112 °C and 370 °C and the primary exothermic peak at 200 °C are caused by decomposition of ammonia, citric acid, and formation of LVP. The subsequent slight weight loss above 370 °C arises from the pyrolysis of the remaining organic compounds.^[30] XPS was performed to investigate the surface chemical state of the samples. Only V, P, O, C, and Na/Cr are detected (Figure 4(b), Table S-I) without impurities, which is consistent with the XRD results. The Na 1s peak at the binding energy of 1070 eV in $\text{Li}_{2.96}\text{Na}_{0.04}\text{V}_2(\text{PO}_4)_3/\text{C}$ confirmed successful doping of Na^+ into the lattice structure of LVP. The XPS of Cr 2p includes the two peaks of Cr 2p_{3/2} and 2p_{1/2} at the energies of 576.7 and 586.5 eV (Figure 4(c)).

The surface area and pore information of $\text{Li}_3\text{V}_2(\text{PO}_4)_3/\text{C}$, $\text{Li}_{3-x}\text{Na}_x\text{V}_2(\text{PO}_4)_3/\text{C}$, and $\text{Li}_3\text{V}_{2-x}\text{Cr}_x(\text{PO}_4)_3/\text{C}$ were measured with the N_2 adsorption/desorption isotherms shown in Figure 5. All samples show a type IV N_2 adsorption-desorption isotherm curve with hysteresis loops, confirming mesoporosity of the as-synthesized samples. The corresponding parameters related to the specific surface area and pore structure are listed in Table II. All doped samples show larger surface areas and pore volumes than the pristine sample, which may be due to the enhanced pore structure stability of materials for buffering the stress induced by crystal growth after metal doping.^[31] Both the LVP composites at the doping level of 0.04 show the largest surface areas of 182.54 $\text{m}^2 \text{g}^{-1}$ for $\text{Li}_{2.96}\text{Na}_{0.04}\text{V}_2(\text{PO}_4)_3/\text{C}$ and 209.77 $\text{m}^2 \text{g}^{-1}$ for $\text{Li}_3\text{V}_{1.96}\text{Cr}_{0.04}(\text{PO}_4)_3/\text{C}$ and the largest surface

areas in micropores and mesopores. According to the pore size distribution plot (shown in the inset), $\text{Li}_{3-x}\text{Na}_x\text{V}_2(\text{PO}_4)_3/\text{C}$ and $\text{Li}_3\text{V}_{2-x}\text{Cr}_x(\text{PO}_4)_3/\text{C}$ consist of the mesopores with the primary size of 4 to 5 nm, which is slightly larger than LVP (3 to 4 nm). The pore volume increases with the addition of Na and Cr dopants to a maximum of 0.245 and 0.445 $\text{cm}^3 \text{g}^{-1}$, respectively, at $x = 0.04$. The hierarchical porous structure with a multidimensional domain at different length scales not only improves the contact area between the electrode and the electrolyte, but also provides many more activity sites for enhancing the electrochemical performances of the materials.^[28] We added surface area ratios of mesopores over micropores in Table II, because mesopores and micropores are the two main pore scales in the materials. It can be seen that doping increased the fraction of mesopores in the materials. The increase in mesopore fraction not only can facilitate an intimate contact between the liquid electrolyte and active LVP/C nanoparticles, but also can accelerate mass and charge transfer. On the other hand, micropores can facilitate Li-ion storage by confining ions within the pores. Macropores can accelerate lithium ion transfer by providing more channels. Therefore, the multimodal porous structure of the materials can effectively alleviate volume change during lithiation/delithiation and promote diffusion kinetics.^[12,32]

Figures 6(a) and (b) present the initial charge/discharge curves of $\text{Li}_{3-x}\text{Na}_x\text{V}_2(\text{PO}_4)_3/\text{C}$ and $\text{Li}_3\text{V}_{2-x}\text{Cr}_x(\text{PO}_4)_3/\text{C}$ cathodes annealed at 850 °C at 0.1 C in the potential range of 3.0 to 4.3 V. Figure S-4(a) shows the charge/discharge curves of undoped LVP/C in the first several cycles at different rates. All samples present three charge/discharge platforms at 4.09, 3.68, and 3.60 V (charge) as well as 4.05, 3.65, and 3.58 V (discharge) in the potential range of 3.0 to 4.3 V, corresponding to the three-stage phase transition within the materials through lithium insertion and extraction.^[33,34] The presence of Na and Cr dopants does not change these platform potential values, indicating that no extra phase transformation occurs. The initial discharge capacity values of $\text{Li}_{3-x}\text{Na}_x\text{V}_2(\text{PO}_4)_3/\text{C}$ are 133.4, 137.3, and 136.5 mAh g^{-1} at $x = 0.03, 0.04,$ and 0.05, respectively, which are slightly higher than those of $\text{Li}_3\text{V}_{2-x}\text{Cr}_x(\text{PO}_4)_3/\text{C}$ of 120.9, 134.6, and 130.4 mAh g^{-1} , respectively, at the same doping levels. Both $\text{Li}_{3-x}\text{Na}_x\text{V}_2(\text{PO}_4)_3/\text{C}$ and $\text{Li}_3\text{V}_{2-x}\text{Cr}_x(\text{PO}_4)_3/\text{C}$ have larger initial capacity values than undoped LVP/C (Figure S-4a), indicating that the introduction of Na and Cr into LVP/C enhanced the capacity of the material. Compared with the doped samples themselves, the maximum capacity values of both $\text{Li}_{3-x}\text{Na}_x\text{V}_2(\text{PO}_4)_3/\text{C}$ and $\text{Li}_3\text{V}_{2-x}\text{Cr}_x(\text{PO}_4)_3/\text{C}$ are achieved at the doping level of $x = 0.04$. The cycling rate performances of $\text{Li}_{3-x}\text{Na}_x\text{V}_2(\text{PO}_4)_3/\text{C}$ and $\text{Li}_3\text{V}_{2-x}\text{Cr}_x(\text{PO}_4)_3/\text{C}$ ($x = 0.03$ and 0.05) are also studied and listed in supplementary Figure S-1. Both the capacity and rate performances of the $\text{Li}_{3-x}\text{Na}_x\text{V}_2(\text{PO}_4)_3/\text{C}$ and $\text{Li}_3\text{V}_{2-x}\text{Cr}_x(\text{PO}_4)_3/\text{C}$ composite cathodes at $x = 0.03$ and 0.05 degraded compared with Na-doped $\text{Li}_{2.96}\text{Na}_{0.04}\text{V}_2(\text{PO}_4)_3/\text{C}$ and Cr-doped $\text{Li}_3\text{V}_{1.96}\text{Cr}_{0.04}(\text{PO}_4)_3/\text{C}$. As discussed previously, doping

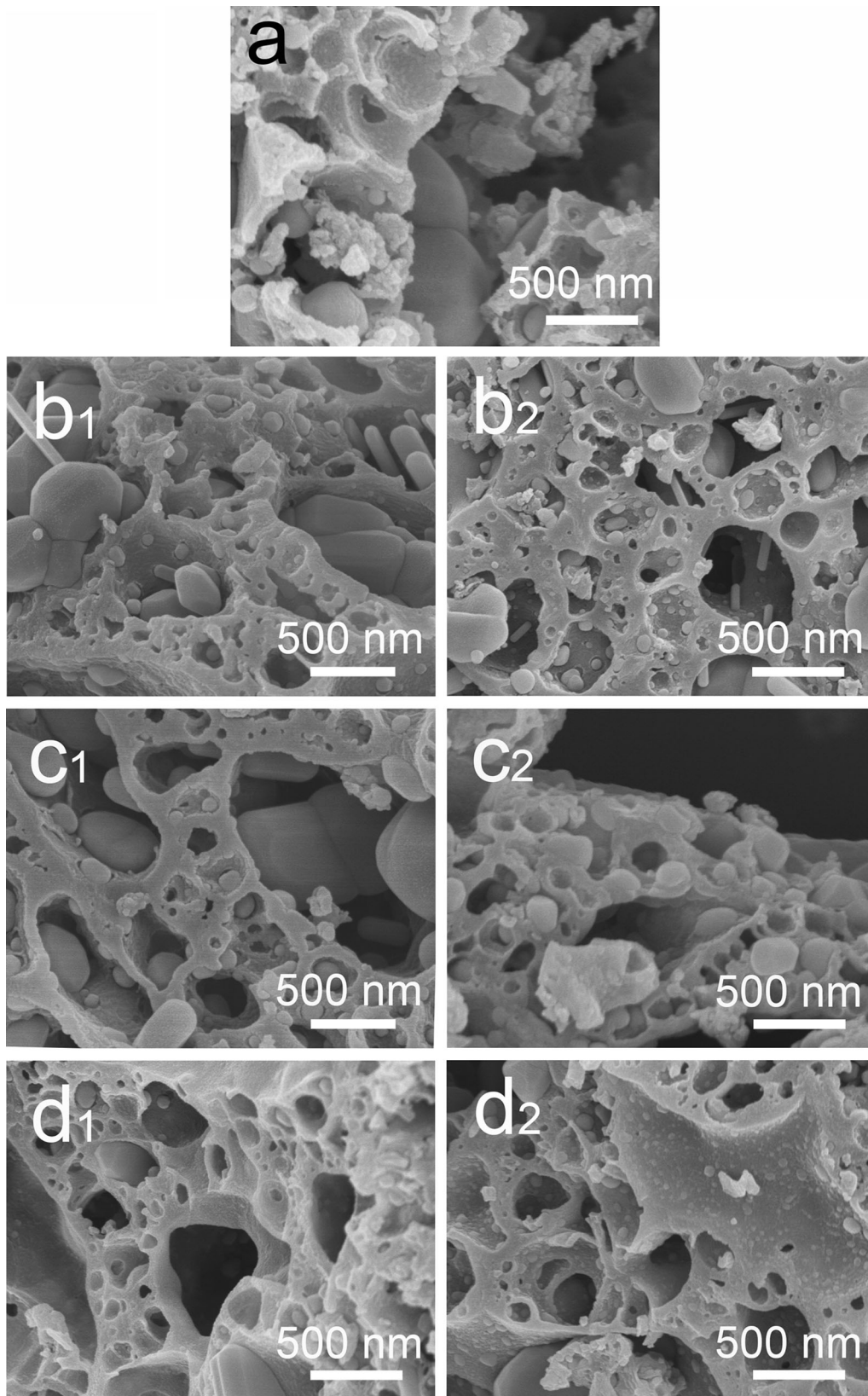


Fig. 2—SEM images of (a) undoped LVP/C and Na- and Cr-doped samples at the doping level of (b1) and (b2) $x = 0.03$, (c1) and (c2) $x = 0.04$, and (d1) and (d2) $x = 0.05$.

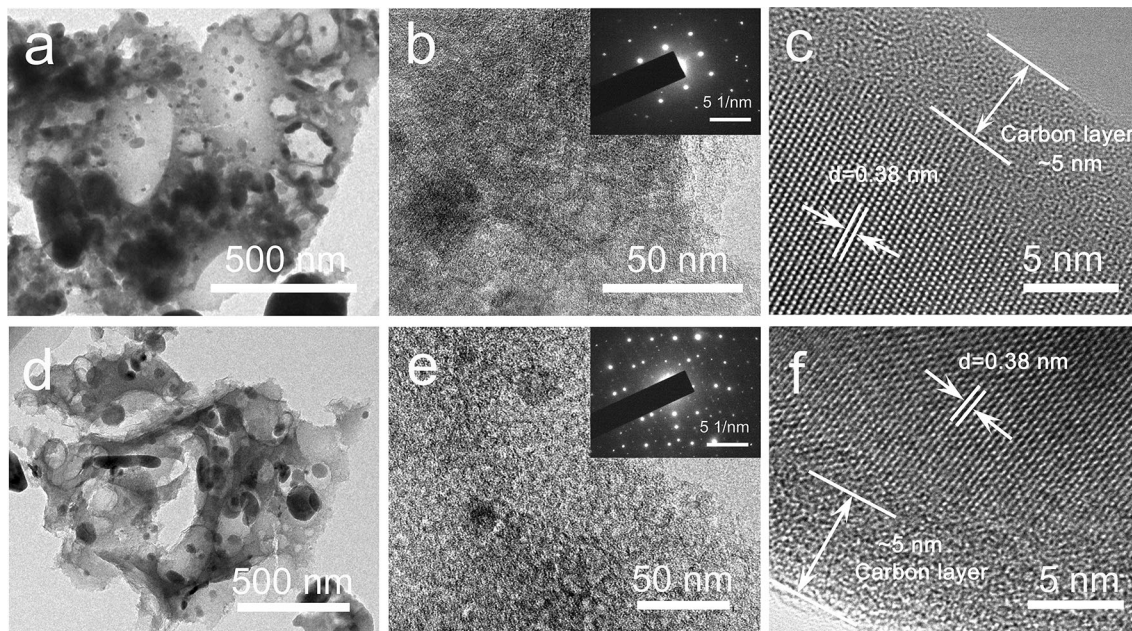


Fig. 3—TEM images of (a) through (c) $\text{Li}_{2.96}\text{Na}_{0.04}\text{V}_2(\text{PO}_4)_3/\text{C}$ and (d) through (f) $\text{Li}_3\text{V}_{1.96}\text{Cr}_{0.04}(\text{PO}_4)_3/\text{C}$ with different magnifications. The inset images are the corresponding SAED patterns.

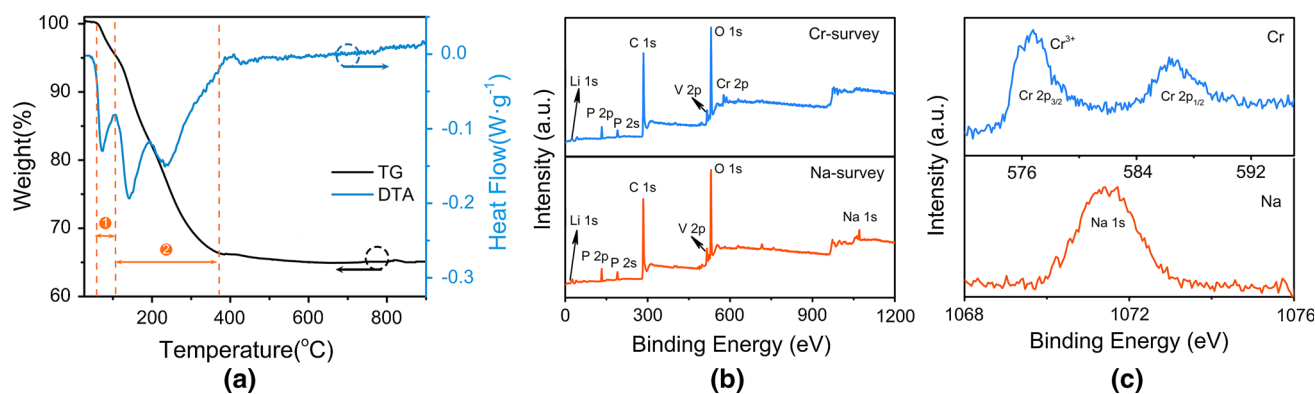


Fig. 4—(a) TG/DTA plots of the LVP/C precursor, (b) XPS spectra of $\text{Li}_{2.96}\text{Na}_{0.04}\text{V}_2(\text{PO}_4)_3/\text{C}$ and $\text{Li}_3\text{V}_{1.96}\text{Cr}_{0.04}(\text{PO}_4)_3/\text{C}$, and (c) XPS peaks of Na 1s and Cr 2p.

increases the electrical conductivity of the as-prepared composite materials, which is beneficial for enhancement in the charge/discharge capacity. In addition, doping influences the pore structure of the composites, as shown in Table II, and an appropriate hierarchical porous framework, including macro-, meso-, and micropores, provides sufficient channels for Li^+ diffusion and reduces the transportation distance. However, when the doping level exceeds the optimum value, the excess Na/Cr dopants may enlarge the crystal size with a decrease in the surface area and introduce more vacancies to decrease the electronic conductivity, which can depress the capacity and the rate capability.^[35,36]

The influence of the annealing temperature on the first cycle charge/discharge capacity and rate performance of $\text{Li}_{2.96}\text{Na}_{0.04}\text{V}_2(\text{PO}_4)_3/\text{C}$ and $\text{Li}_3\text{V}_{1.96}\text{Cr}_{0.04}(\text{PO}_4)_3/\text{C}$ was also investigated (supplementary Figure S-2). The initial capacity increases with increasing annealing

temperatures and then decreases at temperatures over 850 $^{\circ}\text{C}$. The sample annealed at 850 $^{\circ}\text{C}$ exhibits the highest initial capacity of 137.3 $\text{mAh}\cdot\text{g}^{-1}$ for $\text{Li}_{2.96}\text{Na}_{0.04}\text{V}_2(\text{PO}_4)_3/\text{C}$ and 134.6 $\text{mAh}\cdot\text{g}^{-1}$ for $\text{Li}_3\text{V}_{1.96}\text{Cr}_{0.04}(\text{PO}_4)_3/\text{C}$, while the corresponding values for peer samples at 800 $^{\circ}\text{C}$ and 900 $^{\circ}\text{C}$ are 126.2/115.8 $\text{mAh}\cdot\text{g}^{-1}$ (Na-doped samples) and 113.9/105.3 $\text{mAh}\cdot\text{g}^{-1}$ (Cr-doped samples). Meanwhile, the rate performance is also improved in samples annealing at 850 $^{\circ}\text{C}$ than those at other temperatures. Crystallinity of the as-prepared materials will be enhanced during increasing temperature, which is beneficial for the increase in electronic conductivity and electrochemical performances. However, an excessively high annealing temperature will destroy the hierarchical porosity, leading to pore collapse and coarsening of materials.^[37–39] An appropriate annealing temperature, therefore, is required to achieve the optimal electrochemical performances of the materials. In addition, we investigated the role of ice

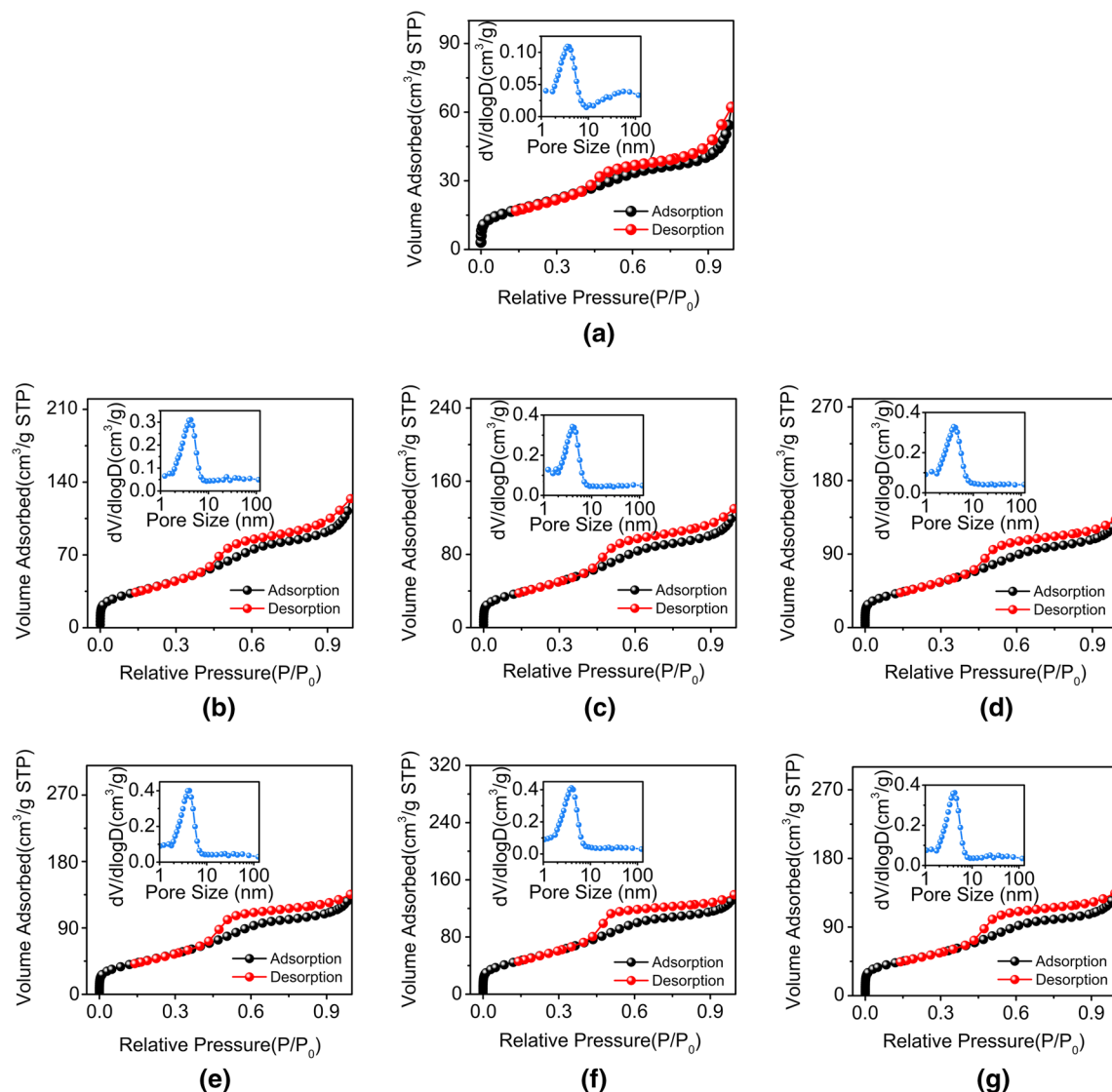


Fig. 5—N₂ adsorption and desorption isotherms of samples (a) Li₃V₂(PO₄)₃/C, (b) through (d) Li_{3-x}Na_xV₂(PO₄)₃/C, and (e) through (g) Li₃V_{2-x}Cr_x(PO₄)₃/C ($x = 0.03, 0.04$ and 0.05). The inset plots are the pore size distributions derived from the Barrett–Joyner–Halenda method.

Table II. Surface Areas and Pore Volumes of All Samples

Sample	S_{BET} (m ² g ⁻¹)	S_{micro} (m ² g ⁻¹)	S_{meso} (m ² g ⁻¹)	$S_{\text{meso}}/S_{\text{micro}}$	V_{pore} (m ³ g ⁻¹)	V_{micro} (m ³ g ⁻¹)	V_{meso} (m ³ g ⁻¹)
LVP/C	66.93	3.86	60.84	15.76	0.096	0.004	0.092
$x(\text{Na}) = 0.03$	154.9	6.89	135.32	19.64	0.192	0.011	0.172
$x(\text{Na}) = 0.04$	182.54	8.01	159.51	19.91	0.245	0.022	0.198
$x(\text{Na}) = 0.05$	174.84	7.26	152.86	21.06	0.21	0.017	0.188
$x(\text{Cr}) = 0.03$	186.37	8.7	167.63	19.27	0.397	0.025	0.215
$x(\text{Cr}) = 0.04$	209.77	10.2	185.54	18.19	0.445	0.034	0.287
$x(\text{Cr}) = 0.05$	175.49	7.35	164.49	23.37	0.385	0.021	0.196

S_{micro} and S_{meso} correspond to surface areas of micropores and mesopores, respectively; V_{pore} is the total pore volume; and V_{micro} and V_{meso} are volumes of micropores and mesopores.

templating on the cycling performance of LVP cathodes, as shown in supplementary Figure S-3. LVP/C synthesized by ice templating shows an outstanding cycling performance with a high capacity (115.4 mAh g⁻¹) after 100 cycles, which is close to reported results^[22] and better than the ones prepared without ice templating (104.6 mAh g⁻¹).

The rate performances of Li_{2.96}Na_{0.04}V₂(PO₄)₃/C, Li₃V_{1.96}Cr_{0.04}(PO₄)₃/C, and pristine LVP/C composite cathodes at different rates are shown in Figure 7(a). Compared with the undoped LVP/C, both doped samples show smaller irreversible capacity losses with an increase in the charge/discharge rate, indicating that

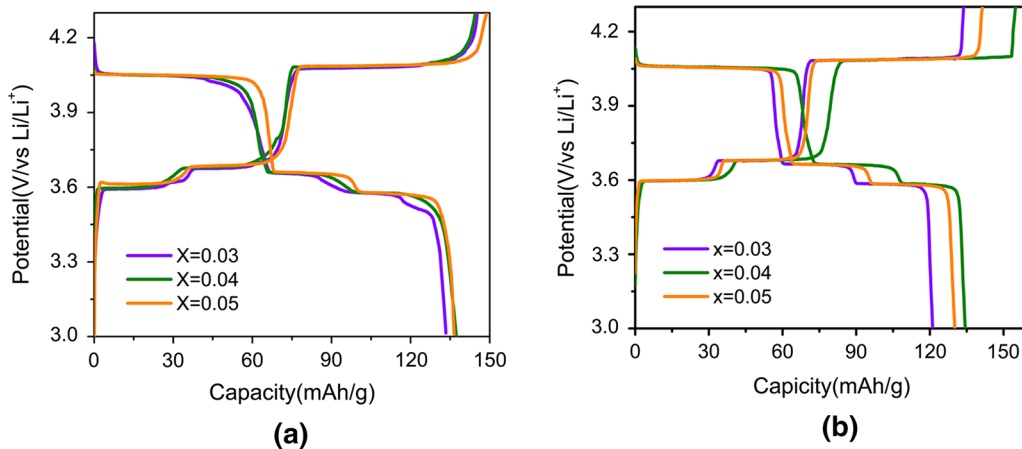


Fig. 6—Initial charge/discharge curves of (a) Na-doped $\text{Li}_{3-x}\text{Na}_x\text{V}_2(\text{PO}_4)_3/\text{C}$ and (b) Cr-doped $\text{Li}_3\text{V}_{2-x}\text{Cr}_x(\text{PO}_4)_3/\text{C}$ at 0.1 C annealed at 850 °C with a doping level of $x = 0.03, 0.04,$ and 0.05 .

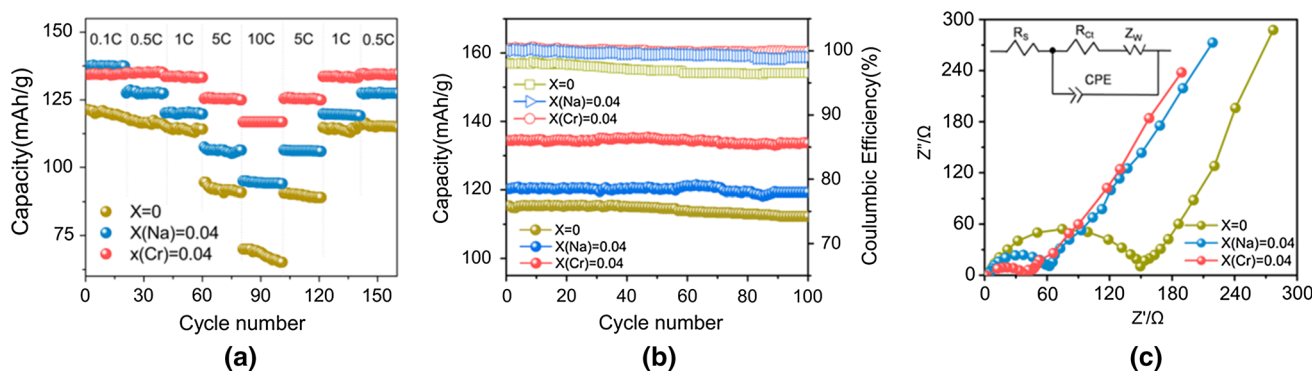


Fig. 7—(a) Rate performances at different rates, (b) discharge capacity and coulombic efficiency of doped and undoped LVP/C during cycles at 1 C, and (c) electrochemical impedance spectra of the samples (the inset is the equivalent circuit used to fit the EIS).

metal doping increases the transportation rate within the framework and facilitates insertion/extraction of Li ions, which results in reduction of electrode polarization as well as enhancement in the rate performance of doped cathodes. The discharge capacities of $\text{Li}_{2.96}\text{Na}_{0.04}\text{V}_2(\text{PO}_4)_3/\text{C}$ and $\text{Li}_3\text{V}_{1.96}\text{Cr}_{0.04}(\text{PO}_4)_3/\text{C}$ are 137.8 and 135.1 mAh g^{-1} at 0.1 C, 128.6 and 134.8 mAh g^{-1} at 0.5 C, 120.4 and 133.7 mAh g^{-1} at 1 C, and 117.6 and 125.9 mAh g^{-1} at 5 C, respectively. Even at 10 C, $\text{Li}_{2.96}\text{Na}_{0.04}\text{V}_2(\text{PO}_4)_3/\text{C}$ and $\text{Li}_3\text{V}_{1.96}\text{Cr}_{0.04}(\text{PO}_4)_3/\text{C}$ maintain high capacities (95 and 116.8 mAh g^{-1} , respectively), which are 71.4/87.9 pct of the theoretical value (133 mAh g^{-1}).^[40,41] In addition, $\text{Li}_3\text{V}_{1.96}\text{Cr}_{0.04}(\text{PO}_4)_3/\text{C}$ shows an excellent high-rate capability with the smallest capacity change. All three samples bounce back to the initial capacity value after rate restoration without apparent decay, confirming the excellent cycle stability and reversibility.

The long-life cycling performance of all samples at 1 C is subsequently tested, and the results are shown in Figure 7(b). The discharge capacity is maintained at 99.1, 99.4, and 96.8 pct after 100 discharge/charge cycles for $\text{Li}_{2.96}\text{Na}_{0.04}\text{V}_2(\text{PO}_4)_3/\text{C}$, $\text{Li}_3\text{V}_{1.96}\text{Cr}_{0.04}(\text{PO}_4)_3/\text{C}$, and LVP/C, respectively (as shown in Table S-II). Both $\text{Li}_{2.96}\text{Na}_{0.04}\text{V}_2(\text{PO}_4)_3/\text{C}$ and $\text{Li}_3\text{V}_{1.96}\text{Cr}_{0.04}(\text{PO}_4)_3/\text{C}$

deliver high discharge capacities of 120.5 and 133.6 mAh g^{-1} after 100 cycles, which are significantly better than most reported state-of-the-art LVP composite cathodes.^[5,33,42–45] The Coulombic efficiencies of $\text{Li}_{2.96}\text{Na}_{0.04}\text{V}_2(\text{PO}_4)_3/\text{C}$ and $\text{Li}_3\text{V}_{1.96}\text{Cr}_{0.04}(\text{PO}_4)_3/\text{C}$ are 99.1 and 99.9 pct for the overall battery operation, indicating that doping enhances the cycling stability of the LVP/C cathode. Doping Na and Cr ions into LVP/C enhances the surface area and improves the structural stability of LVP/C because metals doped into pore walls buffer the stress induced by crystal growth and volume change during lithiation/delithiation, resulting in an increase in coulombic efficiency.

The Nyquist plots of the EIS of the samples shown in Figure 7(c) include semicircles in the high-frequency region and inclined lines in the low-frequency region. Inclined lines in the low-frequency region are related to solid-state diffusion of lithium ions in the active materials.^[46,47] The interception values with the real axis of the semicircles in the high-frequency region represent the charge transfer resistance (R_{ct}) between the active materials and the electrolyte.^[48,49] EIS was simulated by ZSimp Win with an equivalent circuit (inset in Figure 7(c)).

Both $\text{Li}_{2.96}\text{Na}_{0.04}\text{V}_2(\text{PO}_4)_3/\text{C}$ and $\text{Li}_3\text{V}_{1.96}\text{Cr}_{0.04}(\text{PO}_4)_3/\text{C}$ show larger slopes and smaller charge transfer

resistances than undoped LVP/C. R_{ct} is 64.1, 41.6, and 145.5 Ω for $\text{Li}_{2.96}\text{Na}_{0.04}\text{V}_2(\text{PO}_4)_3/\text{C}$, $\text{Li}_3\text{V}_{1.96}\text{Cr}_{0.04}(\text{PO}_4)_3/\text{C}$, and undoped LVP/C, respectively.

The cyclic voltammetry curves of the samples at various scanning rates were measured to reveal the diffusion coefficients of Li ions in the materials. Three couples of oxidation and reduction peaks in the cyclic voltammetry curves are observed in all samples (Figure 8), corresponding to the three charge/discharge steps of the materials. For undoped LVP/C, the peaks at 3.63 and 3.72 V correspond to extraction of the first Li^+ in two steps, confirming the existence of the ordered $\text{Li}_{2.5}\text{V}_2(\text{PO}_4)_3$ intermediate phase and $\text{Li}_2\text{V}_2(\text{PO}_4)_3$ phase. The second Li^+ is extracted through one step at 4.14 V to form $\text{LiV}_2(\text{PO}_4)_3$, corresponding to complete oxidation of V^{3+} to V^{4+} . Three reduction peaks located at 3.52, 3.60, and 3.98 V result from insertion of the two Li^+ ions from the $\text{V}^{4+}/\text{V}^{3+}$ redox couple.^[50,51] Based on the cyclic voltammetry curves in Figure 8, the diffusion coefficients of Li ion (D_{Li}) in the composite cathodes can be estimated according to the following equation:^[52]

$$I_p = 2.69 \times 10^5 n^3/2 AD^{1/2} v^{1/2} C \quad [1]$$

where n is the number of transferred electrons in the electrode reaction, A is the electrode area (1.76 cm^2 in this work), C is the Li-ion concentration, I_p is the peak current intensity (A), and v is the scan rate (V s^{-1}). Among the three steps of Li-ion insertion and extraction, the current densities of oxidation and reduction peaks during the last step are used to calculate the diffusion coefficient. The insets in Figure 8 present the linear relationships between current densities (I_p) of the oxidation and reduction peak and $v^{1/2}$. The Li-ion diffusion coefficients in $\text{Li}_{2.96}\text{Na}_{0.04}\text{V}_2(\text{PO}_4)_3/\text{C}$ and $\text{Li}_3\text{V}_{1.96}\text{Cr}_{0.04}(\text{PO}_4)_3/\text{C}$ are calculated to be 8.8×10^{-11} and 9.4×10^{-11} cm s^{-2} , respectively, and are significantly higher than that of LVP/C (5.0×10^{-11} cm s^{-2}), showing that metal doping leads to faster Li-ion diffusion rates while divalent metal doping shows an even larger improvement. The undoped LVP/C cathode shows a left shift in anodic peaks and a right shift in cathodic peaks in the cyclic voltammetry curves

(supplementary Figure S-5) due to its smaller conductivity and Li-ion diffusion coefficient.

For clear observation, the CV curves of LVP/C, $\text{Li}_{2.96}\text{Na}_{0.04}\text{V}_2(\text{PO}_4)_3/\text{C}$, and $\text{Li}_3\text{V}_{1.96}\text{Cr}_{0.04}(\text{PO}_4)_3/\text{C}$ at 0.3 mV s^{-1} are shown in supplementary Figure S-5. Both oxidation peaks of $\text{Li}_{2.96}\text{Na}_{0.04}\text{V}_3/\text{C}$ and $\text{Li}_3\text{V}_2(\text{PO}_{4.196}\text{Cr}_{0.04}(\text{PO}_4)_3/\text{C}$ shifted down from 4.22, 3.81, and 3.71 to 4.15, 3.73, and 3.65, while the reduced peaks shifted up from 3.89, 3.54, and 3.46 to 3.97, 3.59, and 3.46 V, respectively. In other words, Na and Cr doping reduces the potential difference of $\text{Li}_3\text{V}_2(\text{PO}_4)_3/\text{C}$ and enhances reversibility of the electrode reaction. Note that the oxidation and reduction peaks of $\text{Li}_{2.96}\text{Na}_{0.04}\text{V}_2(\text{PO}_4)_3/\text{C}$ and $\text{Li}_3\text{V}_{1.96}\text{Cr}_{0.04}(\text{PO}_4)_3/\text{C}$ have slightly higher intensities than those of $\text{Li}_3\text{V}_2(\text{PO}_4)_3/\text{C}$. The smaller charge transfer resistance and larger Li ion diffusion coefficient are the most important attributes for the outstanding electrochemical performances of doped samples.

To study the charge storage mechanism of LVP/C, we investigated the relationship between current (I) and scan rate (v) according to the cyclic voltammetry (CV) at different scan rates according to the following power law equation:

$$I = av^b \quad [2]$$

where I is the current, v is the scanning rate, and a and b are the fitting parameters that can be determined from the curve. The value of b is considered to determine the charge storage kinetics, while the process is either diffusion controlled ($b = 0.5$) or entirely dominated by the surface capacitance ($b = 1$).^[53,54]

Figures 9(a) through (c) present the b values at different potentials in the range of 3.5 to 4.1 V, with the fitting variance (R^2) listed. The insets are the current response plotted against scan rates at 3.72, 3.98, 4.02, and 4.16 V. According to the figure, all three samples show similar b -value ranges (from 0.5 to 1.0). The b values of approximately 0.55 in the potential range of 3.5 to 4.0 V and over 0.8 in the other potential range indicate that the charge storage process of the nanocomposites is diffusion controlled in the potential range of 3.5 to 4.0 V and surface capacitive controlled in the other potential region. The ratio of surface capacitive

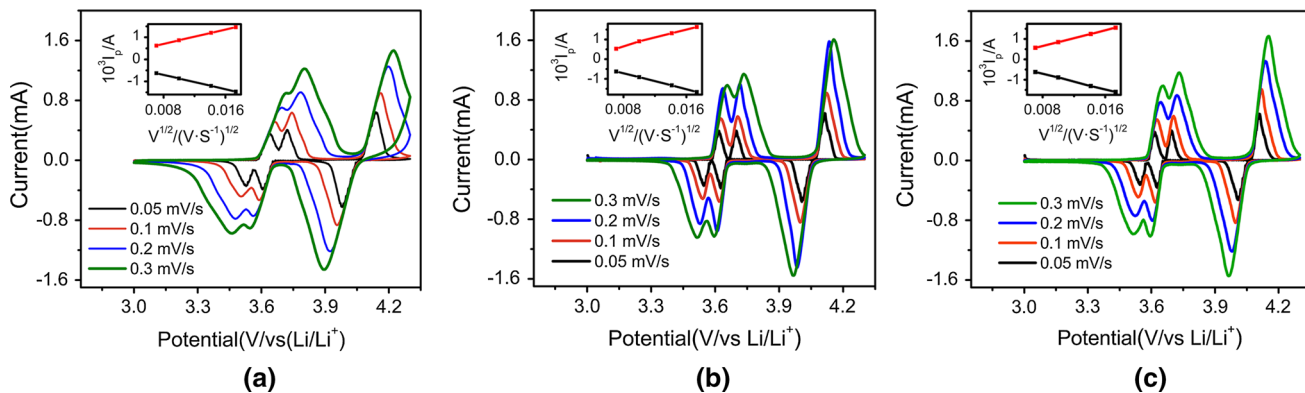


Fig. 8—Cyclic voltammetry curves of (a) $\text{Li}_3\text{V}_2(\text{PO}_4)_3/\text{C}$, (b) $\text{Li}_{2.96}\text{Na}_{0.04}\text{V}_2(\text{PO}_4)_3/\text{C}$, and (c) $\text{Li}_3\text{V}_{1.96}\text{Cr}_{0.04}(\text{PO}_4)_3/\text{C}$ at various scanning rates in the potential range of 3 to 4.3 V. The insets are the corresponding linear relations between I_p and $v^{1/2}$.

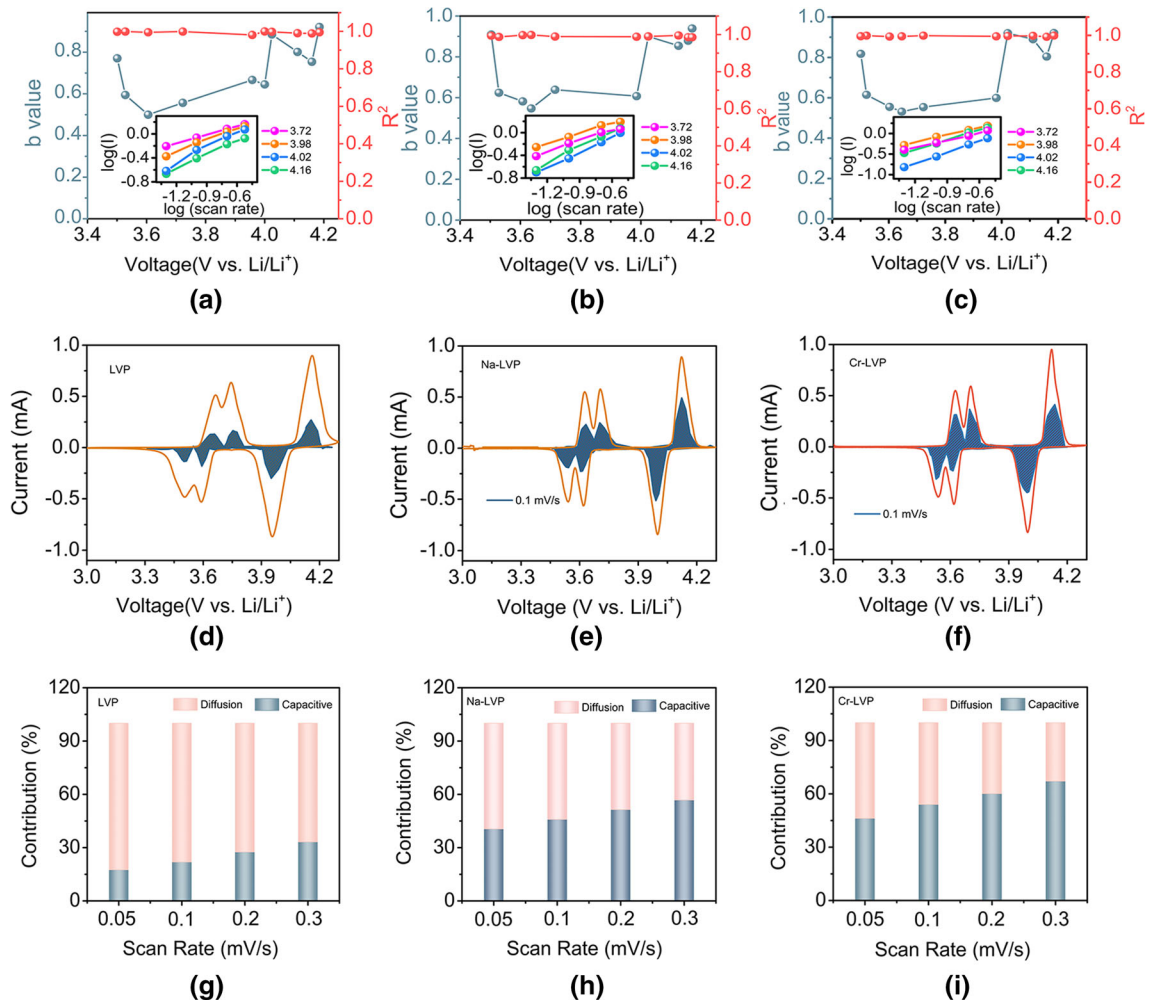


Fig. 9—(a), (b), and (c) Values of (b) plotted at different potentials for $\text{Li}_3\text{V}_2(\text{PO}_4)_3/\text{C}$, $\text{Li}_{2.96}\text{Na}_{0.04}\text{V}_2(\text{PO}_4)_3/\text{C}$, and $\text{Li}_3\text{V}_{1.96}\text{Cr}_{0.04}(\text{PO}_4)_3/\text{C}$, respectively. The inset is the current response plotted against scan rates. (d), (e), and (f) Capacitive (dark blue) and diffusion-controlled (orange) contributions of $\text{Li}_3\text{V}_2(\text{PO}_4)_3/\text{C}$, $\text{Li}_{2.96}\text{Na}_{0.04}\text{V}_2(\text{PO}_4)_3/\text{C}$, and $\text{Li}_3\text{V}_{1.96}\text{Cr}_{0.04}(\text{PO}_4)_3/\text{C}$, respectively, at 0.1 mV s^{-1} . (g), (h), and (i) Normalized contribution ratios of capacitive (dark blue) and diffusion-controlled (orange) capacities for $\text{Li}_3\text{V}_2(\text{PO}_4)_3/\text{C}$, $\text{Li}_{2.96}\text{Na}_{0.04}\text{V}_2(\text{PO}_4)_3/\text{C}$, and $\text{Li}_3\text{V}_{1.96}\text{Cr}_{0.04}(\text{PO}_4)_3/\text{C}$ at different scan rates, respectively (Color figure online).

contribution and diffusion-controlled contribution can be further quantified by the following exponential relationship with the scan rate^[55]:

$$I(V) = k_1 v + k_2 v^{1/2} \quad [3]$$

where v is the sweep rate and $k_1 v$ and $k_2 v^{1/2}$ represent the fraction of the current (I) arising from diffusion and capacitive processes at the potential of V . Figures 9(d), (e), and (f) showed the capacitive current (dark blue) and the diffusion-controlled current (orange) of $\text{Li}_3\text{V}_2(\text{PO}_4)_3/\text{C}$, $\text{Li}_{2.96}\text{Na}_{0.04}\text{V}_2(\text{PO}_4)_3/\text{C}$, and $\text{Li}_3\text{V}_{1.96}\text{Cr}_{0.04}(\text{PO}_4)_3/\text{C}$ at a sweep rate of 0.1 mV s^{-1} . The surface capacitive contributions of $\text{Li}_3\text{V}_2(\text{PO}_4)_3/\text{C}$, $\text{Li}_{2.96}\text{Na}_{0.04}\text{V}_2(\text{PO}_4)_3/\text{C}$, and $\text{Li}_3\text{V}_{1.96}\text{Cr}_{0.04}(\text{PO}_4)_3/\text{C}$ at 0.1 mV s^{-1} are calculated to be 21.9, 45.9, and 54 pct, respectively. With an increase in the scan rate, the capacitive contributions in all samples rise with a maximum value of 67.1 pct achieved at 0.3 mV s^{-1} for $\text{Li}_3\text{V}_{1.96}\text{Cr}_{0.04}(\text{PO}_4)_3/\text{C}$. Capacitive contributions increase with the scan rate, while the value in $\text{Li}_{2.96}\text{Na}_{0.04}\text{V}_2(\text{PO}_4)_3/\text{C}$

is relatively smaller compared with Cr-doped samples. In addition, the capacitive contribution in $\text{Li}_3\text{V}_2(\text{PO}_4)_3/\text{C}$ is significantly lower than those in $\text{Li}_{2.96}\text{Na}_{0.04}\text{V}_2(\text{PO}_4)_3/\text{C}$ and $\text{Li}_3\text{V}_{1.96}\text{Cr}_{0.04}(\text{PO}_4)_3/\text{C}$ at the same scan rates, indicating that metal doping in $\text{Li}_3\text{V}_2(\text{PO}_4)_3/\text{C}$ improves the rate capability due to the higher capacitive contribution that enables faster Li^+ /ion transportation.

Overall, two interesting protocols were shown in the current work. The first one is to synthesize the three-dimensional hierarchical porous $\text{Li}_3\text{V}_2(\text{PO}_4)_3/\text{C}$ composite cathodes with a feasible ice templating method. The as-prepared materials included trimodal macro-, meso-, and micropores in the same structure to take advantage of the synergistic effect between pores at different length scales. Pores with different dimensions serve different and indispensable roles in high electrochemical performances. Macropores buffer the ions as reservoirs to promote mass transportation by shortening the diffusion distance. Mesopores reduce the transfer resistances through diffusion and provide more active sites for the active materials to contact with the electrolyte.

Micropores enhance the electric double layer capacitance by confining ions within the pores.^[56] In addition, carbon is also mixed with the raw materials for LVP synthesis at the molecular level, which is used to improve the conductivity of the cathode materials and to serve as the interconnected buffer cushion to alleviate the volume change during lithium insertion/desertion.^[57] This protocol shortens the transportation distance of electrons between LVP and carbon and reduces the interface barrier for charge carrier transfer. On this basis, metal doping in a moderate level further improves the electrochemical performances, including the capacity and rate capacities of LVP/C composite cathodes for LIBs, by increasing the surface area with formation of a more appropriate hierarchical porous structure. Meanwhile, replacement of Na and Cr with different radii from host ions in $\text{Li}_3\text{V}_2(\text{PO}_4)_3$ changes the lattice constants and cell volumes of the active materials without participating in the redox reactions. As a result, the structural stability during the insertion/desertion process is improved and the cycling performances of the active materials are enhanced. During this process, Na as a dopant substitutes Li^+ and forms $\text{Li}_{3-x}\text{Na}_x\text{V}_2(\text{PO}_4)_3/\text{C}$. The substitution enlarges the cell volume of pristine $\text{Li}_3\text{V}_2(\text{PO}_4)_3/\text{C}$ due to the larger radius of Na^+ . The expansion in the cell volume provides a larger channel for Li^+ diffusion and reduces the resistance of Li^+ insertion and extraction, resulting in the improvement of the electrochemical performances of $\text{Li}_3\text{V}_2(\text{PO}_4)_3/\text{C}$ nanocomposites.^[58] Cr has a smaller ion radius and stronger bonding force with O than V and is more likely to occupy the V sites in $\text{Li}_3\text{V}_2(\text{PO}_4)_3/\text{C}$. Cr doping results in cell volume shrinking of LVP/C and weakens the interaction between Li and O, leading to an enhanced mobility of Li^+ in the $\text{Li}_3\text{Cr}_{0.04}\text{V}_{1.97}(\text{PO}_4)_3/\text{C}$ composites.^[25,59] The electrochemical performances of metal-doped LVP/C composite materials depend on the dopant content with the highest discharge capacity and cycling/rate capabilities achieved at the doping level of $x = 0.04$. The addition of Cr and Na increases the ionic and electronic conductivity of LVP/C in different degrees as well as changes the surface area. Correspondingly, doping alters the cation distribution and reduces use of V through lithium insertion/desertion.^[60] Those balancing effects may explain why a moderate doping level is beneficial for optimal electrochemical performance.

IV. CONCLUSIONS

The Na- and Cr-doped hierarchical porous $\text{Li}_3\text{V}_2(\text{PO}_4)_3/\text{C}$ composites, including trimodal pores, were synthesized by a simple and feasible ice-templating method. The addition of Na and Cr dopants leads to a change in the lattice structure as well as the conductivity of LVP/C. The optimal electrochemical performances at the doping level of $x = 0.04$ are achieved for both Na-doped $\text{Li}_{2.96}\text{Na}_{0.04}\text{V}_2(\text{PO}_4)_3/\text{C}$ and Cr-doped $\text{Li}_3\text{V}_{1.96}\text{Cr}_{0.04}(\text{PO}_4)_3/\text{C}$ with high discharge/charge capacities, excellent rate capabilities, and great cycling performances. Na-doped $\text{Li}_{2.96}\text{Na}_{0.04}\text{V}_2(\text{PO}_4)_3/\text{C}$ possesses

a discharge capacity of 137.8 mAh g^{-1} at 0.1 C and 99.6 mAh g^{-1} at 10 C in the same potential range. Cr-doped $\text{Li}_3\text{V}_{1.96}\text{Cr}_{0.04}(\text{PO}_4)_3/\text{C}$ possesses a discharge capacity of 134.4 mAh g^{-1} at 0.1 C and 117 mAh g^{-1} at 10 C in the potential range of 3 to 4.3 V. Capacity retention can be maintained as 99 pct even after 100 discharge/charge cycles at the rate of 1 C. The charge storage mechanism for all samples is investigated, while the addition of metal dopants leads to an increase in the capacitive contribution at the same scan rate compared with undoped samples. The present work proposed a versatile method for fabrication of metal-doped hierarchical porous materials with trimodal pores and developed the understanding of the influence of metal dopants on the morphology, microstructure, and electrochemical performances of LVP/C-based composites, providing insights into the design of high-performance cathodes for LIBs.

ACKNOWLEDGMENT

This work was supported by the National Natural Science Foundation of China (Grant No. 51574062).

CONFLICT OF INTEREST

The authors express no conflict of interest.

ELECTRONIC SUPPLEMENTARY MATERIAL

The online version of this article (<https://doi.org/10.1007/s11661-018-5075-4>) contains supplementary material, which is available to authorized users.

REFERENCES

1. Y. Cheng, K. Feng, W. Zhou, H. Zhang, X. Li, and H. Zhang: *Dalton Trans.*, 2015, vol. 44, pp. 17579–86.
2. D. Bhuvanewari and N. Kalaiselvi: *Dalton Trans.*, 2014, vol. 43, pp. 18097–18103.
3. L. Mai, S. Li, Y. Dong, Y. Zhao, Y. Luo, and H. Xu: *Nanoscale*, 2013, vol. 5, pp. 4864–69.
4. Y. Chen, Y. Zhao, X. An, J. Liu, Y. Dong, and L. Chen: *Electrochim. Acta*, 2009, vol. 54, pp. 5844–50.
5. D.-W. Han, S.-J. Lim, Y.-I. Kim, S.H. Kang, Y.C. Lee, and Y.-M. Kang: *Chem. Mater.*, 2014, vol. 26, pp. 3644–50.
6. B. Xu, C.R. Fell, M. Chi, and Y.S. Meng: *Energy Environ. Sci.*, 2011, vol. 4, pp. 2223–33.
7. M.-S. Choi, H.-S. Kim, Y.-M. Lee, and B.-S. Jin: *J. Mater. Chem. A*, 2014, vol. 2, pp. 7873–79.
8. C. Wang, Z. Li, H. Liu, and Y. Wang: *New J. Chem.*, 2017, vol. 41, pp. 8772–80.
9. S.-C. Yin, H. Grondy, P. Strobel, M. Anne, and L.F. Nazar: *J. Am. Chem. Soc.*, 2003, vol. 125, pp. 10402–11.
10. A.R. Cho, J.N. Son, V. Aravindan, H. Kim, K.S. Kang, W.S. Yoon, W.S. Kim, and Y.S. Lee: *J. Mater. Chem.*, 2012, vol. 22, pp. 6556–60.

11. C. Sun, S. Rajasekhara, Y. Dong, and J.B. Goodenough: *ACS Appl. Mater. Interfaces*, 2011, vol. 3, pp. 3772–76.
12. L. Fei, L. Sun, W. Lu, M. Guo, H. Huang, J. Wang, H.L. Chan, S. Fan, and Y. Wang: *Nanoscale*, 2014, vol. 6, pp. 12426–33.
13. L.-L. Zhang, G. Liang, G. Peng, F. Zou, Y.-H. Huang, M.C. Croft, and A. Ignatov: *J. Phys. Chem. C*, 2012, vol. 116, pp. 12401–08.
14. K. Naoi, K. Kisu, E. Iwama, Y. Sato, M. Shinoda, N. Okita, and W. Naoi: *J. Electrochem. Soc.*, 2015, vol. 162, pp. A827–33.
15. K. Cui, S. Hu, and Y. Li: *Electrochim. Acta*, 2016, vol. 210, pp. 45–52.
16. Z. Li, L.-L. Zhang, X.-L. Yang, H.-B. Sun, Y.-H. Huang, and G. Liang: *RSC Adv.*, 2016, vol. 6, pp. 10334–40.
17. Q. Kuang, Y. Zhao, and Z. Liang: *J. Power Sources*, 2011, vol. 196, pp. 10169–75.
18. C. Dai, Z. Chen, H. Jin, and X. Hu: *J. Power Sources*, 2010, vol. 195, pp. 5775–79.
19. W. Wang, J. Zhang, Z. Jia, C. Dai, Y. Hu, J. Zhou, and Q. Xiao: *Phys. Chem. Chem. Phys.*, 2014, vol. 16, pp. 13858–65.
20. K. Feng, Y. Cheng, M. Wang, H. Zhang, X. Li, and H. Zhang: *J. Mater. Chem. A*, 2015, vol. 3, pp. 19469–75.
21. H. Liu, P. Gao, J. Fang, and G. Yang: *Chem. Commun.*, 2011, vol. 47, pp. 9110–12.
22. C. Wang, H. Liu, and W. Yang: *J. Mater. Chem.*, 2012, vol. 22, pp. 5281–85.
23. A. Pan, J. Liu, J.-G. Zhang, W. Xu, G. Cao, Z. Nie, B.W. Arey, and S. Liang: *Electrochem. Commun.*, 2010, vol. 12, pp. 1674–77.
24. Y. Luo, X. Xu, Y. Zhang, Y. Pi, Y. Zhao, X. Tian, Q. An, Q. Wei, and L. Mai: *Adv. Energy Mater.*, 2014, vol. 4, pp. 1400107–14.
25. R.-G. Oh, J.-E. Hong, H.-W. Jung, and K.-S. Ryu: *J. Power Sources*, 2015, vol. 295, pp. 1–8.
26. Q.-Z. Ou, Y. Tang, Y.-J. Zhong, X.-D. Guo, B.-H. Zhong, L. Heng, and M.-Z. Chen: *Electrochim. Acta*, 2014, vol. 137, pp. 489–96.
27. Q. Qu, L. Fu, X. Zhan, D. Samuelis, J. Maier, L. Li, S. Tian, Z. Li, and Y. Wu: *Energy Environ. Sci.*, 2011, vol. 4, pp. 3985–90.
28. S. Wang, Z. Zhang, S. Fang, L. Yang, C. Yang, and S.-I. Hirano: *Electrochim. Acta*, 2013, vol. 111, pp. 685–90.
29. H. Li, X. Yu, Y. Bai, F. Wu, C. Wu, L.-Y. Liu, and X.-Q. Yang: *J. Mater. Chem. A*, 2015, vol. 3, pp. 9578–86.
30. R. Zhang, Y. Zhang, K. Zhu, F. Du, Q. Fu, X. Yang, Y. Wang, X. Bie, G. Chen, and Y. Wei: *ACS Appl. Mater. Interfaces*, 2014, vol. 6, pp. 12523–30.
31. J.B.Y.A.X.P. Zhao: *J. Phys. Chem. B*, 2006, vol. 110, pp. 12916–25.
32. C. Wei, W. He, X. Zhang, F. Xu, Q. Liu, C. Sun, and X. Song: *RSC Adv.*, 2015, vol. 5, pp. 54225–45.
33. Q. Wei, Q. An, D. Chen, L. Mai, S. Chen, Y. Zhao, K.M. Hercule, L. Xu, A. Minhas-Khan, and Q. Zhang: *Nano Lett.*, 2014, vol. 14, pp. 1042–48.
34. J. Su, X.-L. Wu, J.-S. Lee, J. Kim, and Y.-G. Guo: *J. Mater. Chem. A*, 2013, vol. 1, pp. 2508–14.
35. N. Meethong, Y.-H. Kao, S.A. Speakman, and Y.-M. Chiang: *Adv. Funct. Mater.*, 2009, vol. 19, pp. 1060–70.
36. S.Y. Chung, J.T. Bloking, and Y.M. Chiang: *Nat. Mater.*, 2002, vol. 1, pp. 123–28.
37. Z. Wang, W. He, X. Zhang, Y. Yue, G. Yang, X. Yi, Y. Wang, and J. Wang: *ChemElectroChem*, 2017, vol. 4, pp. 671–78.
38. P. Fu, Y. Zhao, Y. Dong, X. An, and G. Shen: *J. Power Sources*, 2006, vol. 162, pp. 651–57.
39. J.-C. Zheng, X.-H. Li, Z.-X. Wang, H.-J. Guo, Q.-Y. Hu, and W.-J. Peng: *J. Power Sources*, 2009, vol. 189, pp. 476–79.
40. C. Wang, W. Shen, and H. Liu: *New J. Chem.*, 2014, vol. 38, pp. 430–36.
41. X. Nan, C. Zhang, C. Liu, M. Liu, Z.L. Wang, and G. Cao: *ACS Appl. Mater. Interfaces*, 2016, vol. 8, pp. 862–70.
42. R. Wang, S. Xiao, X. Li, J. Wang, H. Guo, and F. Zhong: *J. Alloys Compd.*, 2013, vol. 575, pp. 268–72.
43. L. Liu, X. Lei, H. Tang, R. Zeng, Y. Chen, and H. Zhang: *Electrochim. Acta*, 2015, vol. 151, pp. 378–85.
44. J. Kim, J.-K. Yoo, Y.S. Jung, and K. Kang: *Adv. Energy Mater.*, 2013, vol. 3, pp. 1004–07.
45. Y. Wang, L. Wang, Z. Hou, and W. Mao: *Solid State Ionics*, 2014, vol. 261, pp. 11–16.
46. Y. Yu, L. Gu, X. Lang, C. Zhu, T. Fujita, M. Chen, and J. Maier: *Adv. Mater.*, 2011, vol. 23, pp. 2443–47.
47. S. Wang, W. Zhao, Y. Wang, X. Liu, and L. Li: *Electrochim. Acta*, 2013, vol. 109, pp. 46–51.
48. S. Yang, X. Feng, and K. Mullen: *Adv. Mater.*, 2011, vol. 23, pp. 3575–79.
49. Y. Zhang, X. Liu, S. Wang, S. Dou, and L. Li: *J. Mater. Chem. A*, 2016, vol. 4, pp. 10869–77.
50. G.C.D. Morgan, M.Y. Saidi, J. Barker, J. Swoyer, H. Huang, and G. Adamson: *Chem. Mater.*, 2002, vol. 14, pp. 4684–93.
51. S. Sarkar and S. Mitra: *J. Phys. Chem. C*, 2014, vol. 118, pp. 11512–25.
52. H. Wang, Y. Li, C. Huang, Y. Zhong, and S. Liu: *J. Power Sources*, 2012, vol. 208, pp. 282–87.
53. J. Liu, J. Wang, C. Xu, H. Jiang, C. Li, L. Zhang, J. Lin, and Z.X. Shen: *Adv. Sci.*, 2018, vol. 5, pp. 1700322–41.
54. J. Wang, J. Polleux, J. Lim, and B. Dunn: *J. Phys. Chem. C*, 2007, vol. 111, pp. 14925–31.
55. C. Zhao, C. Yu, M. Zhang, H. Huang, S. Li, X. Han, Z. Liu, J. Yang, W. Xiao, J. Liang, X. Sun, and J. Qiu: *Adv. Energy Mater.*, 2017, vol. 7, pp. 1602880–87.
56. D.W. Wang, F. Li, M. Liu, G.Q. Lu, and H.-M. Cheng: *Angew. Chem.*, 2008, vol. 120, pp. 379–82.
57. Y. Yu, L. Gu, C. Zhu, S. Tsukimoto, P.A. van Aken, and J. Maier: *Adv. Mater.*, 2010, vol. 22, pp. 2247–50.
58. Q. Chen, X. Qiao, Y. Wang, T. Zhang, C. Peng, W. Yin, and L. Liu: *J. Power Sources*, 2012, vol. 201, pp. 267–73.
59. W. Yuan, J. Yan, Z. Tang, O. Sha, J. Wang, W. Mao, and L. Ma: *Electrochim. Acta*, 2012, vol. 72, pp. 138–42.
60. C. Deng, S. Zhang, S.Y. Yang, Y. Gao, B. Wu, L. Ma, B.L. Fu, Q. Wu, and F.L. Liu: *J. Phys. Chem. C*, 2011, vol. 115, pp. 15048–56.